A COMPARATIVE STUDY OF POROUS MEDIA MODELS IN A DIFFERENTIALLY HEATED SQUARE CAVITY USING A FINITE ELEMENT METHOD

D. MISRA AND A. SARKAR

Application Software R & D Laboratory, Department of Mechanical Engineering, Jadavpur University, Calcutta 700 032, India

ABSTRACT

A comparative study is made between different flow models for analysis of natural convection in a differentially heated vertical square cavity filled with a fluid saturated porous medium. The solution is obtained by using a finite element method. The Darcy-modified Rayleigh number, Ra^*, is varied from 50 to 1000 while the Darcy number, Da, ranges from 5×10^{-7} to 10^{-2}. It is generally observed that for small values of Ra^* and Da, all other models converge with the Darcy flow model. However, for large values of Ra^* and Da, the Darcy flow model predicts the highest heat transfer rate, and the Brinkman-Forchheimer extension yields the lowest heat transfer rate whilst prediction from the Brinkman-extended model lies in between.

KEY WORDS   Natural convection   Porous media   Finite element method

NOMENCLATURE

A	dimensionless constant	T	temperature
B	dimensionless constant	T_c	temperature at the cold wall
c	isobaric specific heat	T_h	Temperature at the hot wall
C	dimensionless constant	ΔT	temperature difference, $(T_h - T_c)$
Da	Darcy number, K/L^2	u	horizontal velocity component
g	gravitational acceleration	$\|u\|$	absolute velocity, $\sqrt{(u^2 + v^2)}$
k	thermal conductivity of the fluid	U	dimensionless horizontal velocity component, $u/\sqrt{g\beta\Delta TL}$
k_{eff}	effective thermal conductivity of the fluid medium	$\|U\|$	dimensionless absolute velocity, $\sqrt{(U^2 + V^2)}$
K	permeability		
L	dimension of the square cavity	v	vertical velocity component
Nu	local Nusselt number	V	dimensionless vertical velocity component, $v/\sqrt{g\beta\Delta TL}$
$\overline{Nu}$	average Nusselt number		
p	pressure	x	horizontal coordinate
Pr	Prandtl number, v/α	X	dimensionless horizontal coordinate, x/L
Ra	Rayleigh number, $g\beta(T_h - T_c)L^3/v\alpha$		
Ra^*	Darcy-modified Rayleigh number, $g\beta(T_h - T_c)KL/v\alpha$	y	vertical coordinate
		Y	dimensionless vertical coordinate, y/L

Greek symbols

α thermal diffusivity, $k/\rho c$

β isobaric coefficient of thermal expansion of the fluid

θ dimensionless temperature, $(T - T_c)/(T_h - T_c)$

μ dynamic viscosity of the fluid

μ_{eff} effective viscosity of the porous medium

ν kinematic viscosity of the fluid, μ/ρ

ρ fluid density

Ψ dimensionless stream function

Ω dimensionless vorticity

Subscripts

c cold wall

h hot wall

INTRODUCTION

Natural convection in porous media finds its application in such diverse areas as geothermal energy extraction, solidification of castings, building insulation etc. Many of these problems can be modelled as the case of natural convection in a differentially heated rectangular enclosure filled with fluid saturated porous media. Comprehensive review in this area is available in Cheng[1].

Theoretical studies on natural convection in porous enclosures are reported in References 2–13. The Darcy equations of motion subjected to an impermeable boundary condition are solved in References 2–8, while extended versions of Darcy's law are treated in References 9–13. Walker and Homsy[2] carried out an asymptotic solution to the Darcy equations to study natural convection in rectangular enclosures. A finite element solution based on the Galerkin formulation was presented by Hickox and Gartling[3] to study heat transfer in a shallow porous cavity. Shiralkar *et al.*[4] reported a numerical study of natural convection and presented correlations of the Nusselt number for different aspect ratios of the cavity. The effect of aspect ratio on flow structure and heat transfer was investigated by Prasad and Kulacki[5]. A detailed study of anisotropic effects of permeability and thermal conductivity on the flow and heat transfer in a square cavity was presented by Ni and Beckermann[6]. Burns *et al.*[7] studied analytically the impact of wall leakage on heat transfer in a porous slot with different thermal boundary conditions. The influence of a thin protrusion from the active wall of a rectangular enclosure on flow patterns and heat transfer was investigated by Bejan[8].

Much earlier than the above-mentioned studies, Chan *et al.*[9] applied the Brinkman-extended Darcy formulation to account for the viscous drag in their study with different aspect ratios of the cavity. Lauriat and Prasad[10] incorporated the transport terms in the Brinkman-extended Darcy equations of motion. They observed that the contribution of the transport terms on the overall heat transfer rate is generally negligible. They encountered convergence difficulties at high values of modified Rayleigh and Darcy numbers, and indicated the incorporation of the Forchheimer extension as a possible remedy. To account for the inertia effect in the inertial flow regime, the Forchheimer-extended Darcy equations subjected to the impermeable boundary condition were adopted by Prasad and Tuntomo[11] and results for high values of the modified Rayleigh number were presented by them. Beckermann *et al.*[12] modelled their analysis on the Brinkman-Forchheimer-extended Darcy equations to study the effects of these extensions. They noted that the relative importance of the inertia term modelled through the Forchheimer extension assumes significance mainly at low Prandtl numbers. They also suggested that both these extensions are equally important for flow in a highly porous medium. The effects of the inertial and viscous forces were further investigated by Lauriat and Prasad[13] via the Brinkman-Forchheimer-extended Darcy equations with the transport terms. The non-Darcian effects on flow and heat transfer were studied and criteria to delimit the non-Darcian flow regime were presented by them.

Apart from the above-mentioned studies, natural convection in layered porous media and layered fluid-porous media were also studied by adopting alternative flow models[14-19]. Poulikakos and Bejan[14] studied natural convection in a vertically and horizontally layered porous media with isothermal side walls. Lai and Kulacki[15] investigated a vertically layered porous cavity with a uniform heat flux imposed on one of the side walls and an isothermal condition on the other side wall. The Darcy flow model was adopted in both of these studies. The Darcy flow model ensures continuity of velocity at the interface of porous layers. However, to ensure matching of the normal and shear stresses at the interface, the Brinkman extension was introduced in References 16-19. Beckermann et al.[16,17] adopted the Brinkman-Forchheimer extensions to study flow and heat transfer in a square cavity with layered fluid and porous zones. The studies by Arquis and Caltagirone[18] and Breton et al.[19] adopted the Brinkman extension with Navier-Stokes type transport terms to study heat transfer in a square cavity with porous layers on the side walls. The Forchheimer extension was neglected in References 18, 19 based on the assumption that the pore diameter based Reynolds number is close to one. Excluding the studies in References 2, 3 and 7, all the works discussed above have been analyzed by a finite difference method.

From the above discussion on some of the reported theoretical studies on natural convection in porous media, it is evident that all possible combinations of Darcy's law with various extensions have been attempted by different authors. Besides, the area suffers from a lack of adequate experimental results. It is in this context, the present authors, while working on another related problem, were faced with the difficulty of adopting the appropriate model and subsequently decided to make the present comparative study on some of the existing models for natural convection in a porous square cavity. In the studies of flow through porous media, Darcy's law occupies the central position. Darcy's law is essentially a balance of the viscous force, gravitational force and pressure gradient. It neglects the inertia effect and, hence, applicable for low velocity. For Reynolds numbers, based on the pore diameter or the square root of the permeability as the length scale, of the order of one, Darcy's law accurately predicts the flow. Detailed discussions on the Darcy flow model are available in References 1, 20-22. For Reynolds numbers exceeding the order of one, the Darcy flow model is found to be inadequate and the Forchheimer extension is proposed. The Forchheimer extension, in the form of a quadratic velocity term, is introduced to take care of the inertia effect[1,22]. On the other hand, for flow through porous medium of large permeability, the flow model is expected to be reduced to the viscous flow limit. Thus, the Brinkman extension is introduced to handle such a situation. The viscosity associated with the momentum diffusion terms may have a different value than the fluid viscosity[1]. Moreover, it ensures the automatic matching of the interfacial stresses for flow through layered porous media of different permeabilities[17]. Extending the same logic of flow through porous media of large permeability, it is argued that in the limiting case, the equations of motion must be reduced to the Navier-Stokes equations. Hence, transport terms are also added along with the Brinkman extension in some cases[10,13,19]. In the models used by Lauriat and Prasad[10,13], the effect of porosity is introduced by dividing the convective terms by the square of the porosity. On the other hand, Breton et al.[19] have simply adopted the convective terms, tacitly adopting the porosity close to unity.

In the present work, a comparative study is made between the Darcy equations, the Brinkman-extended Darcy equations, the Brinkman-extended Darcy equations with Navier-Stokes type transport terms and the Brinkman-Forchheimer-extended Darcy equations to explore natural convection in a square cavity with differentially heated isothermal side walls and adiabatic horizontal walls. For the Darcy flow model, the impermeable wall boundary condition and for the Brinkman extended models, the impermeable and no-slip boundary conditions are imposed on the walls. A solution to the system of conservation equations is obtained by a finite element method. The Newton-Raphson algorithm is adopted to achieve rapid convergence.

ANALYSIS

Problem geometry and model equations

The problem geometry considered is a square cavity with L as the length of each side (refer to *Figure 1*). The left and right vertical walls are maintained at T_c and T_h ($T_h > T_c$) respectively, while the top and bottom walls are adiabatic. The cavity is filled with an isotropic and homogeneous porous medium, saturated with air. All the thermophysical properties are constant except the density variation in the body force term which obeys the Boussinesq approximation. Considering steady, two-dimensional flow, the governing equations are:

$$\frac{\partial u}{\partial x} + \frac{\partial v}{\partial y} = 0 \tag{1}$$

$$A\rho\left(u\frac{\partial u}{\partial x} + v\frac{\partial u}{\partial y}\right) + \frac{\mu}{K}u = -\frac{\partial p}{\partial x} + B\mu_{\text{eff}}\left(\frac{\partial^2 u}{\partial x^2} + \frac{\partial^2 u}{\partial y^2}\right) - \frac{C\rho}{\sqrt{K}}|u|u \tag{2}$$

$$A\rho\left(u\frac{\partial v}{\partial x} + v\frac{\partial v}{\partial y}\right) + \frac{\mu}{K}v = -\frac{\partial p}{\partial y} + B\mu_{\text{eff}}\left(\frac{\partial^2 v}{\partial x^2} + \frac{\partial^2 v}{\partial y^2}\right) - \frac{C\rho}{\sqrt{K}}|u|v + \rho g\beta(T - T_c) \tag{3}$$

$$\rho c\left(u\frac{\partial T}{\partial x} + v\frac{\partial T}{\partial y}\right) = k_{\text{eff}}\left(\frac{\partial^2 T}{\partial x^2} + \frac{\partial^2 T}{\partial y^2}\right) \tag{4}$$

where $|u| = \sqrt{(u^2 + v^2)}$ and u and v are velocity components in the x and y directions, and p and T are pressure and temperature, respectively. ρ, μ, c and β are density, viscosity, specific heat at constant pressure and coefficient of thermal expansion of the fluid, respectively. K is the permeability of the porous matrix. μ_{eff} and k_{eff} are effective viscosity and thermal conductivity, respectively. In the present study we have assumed $\mu_{\text{eff}} = \mu$ and $k_{\text{eff}} = k$.

A, B and C are constants such that:

$A = 0, B = 0, C = 0$ for the Darcy flow equations (Model I)

$A = 0, B = 1, C = 0$ for the Brinkman-extended Darcy equations (Model II)

$A = 1, B = 1, C = 0$ for the Brinkman-extended Darcy equations with Navier-Stokes type transport terms (Model III)

$A = 0, B = 1, C = 0.55$ for the Brinkman-Forchheimer-extended Darcy equations (Model IV)
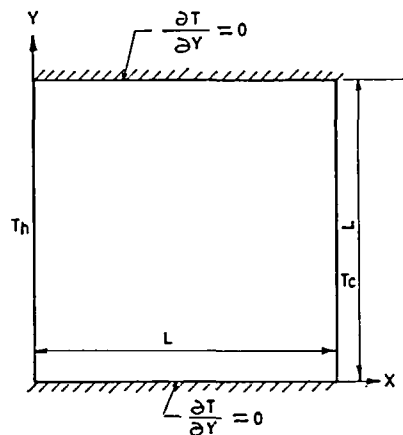

Figure 1   Problem geometry

Defining the following dimensionless variables:

$$(X, Y) = \frac{(x, y)}{L}, \qquad (U, V) = \frac{(u, v)}{\sqrt{(g\beta\Delta T L)}}, \qquad P = \frac{p - p_{ref}}{\rho g\beta(\Delta T)L}, \qquad \theta = \frac{T - T_c}{\Delta T}$$

the following dimensionless forms of the conservation equations are obtained:

$$\frac{\partial U}{\partial X} + \frac{\partial V}{\partial Y} = 0 \tag{5}$$

$$A\left(U\frac{\partial U}{\partial X} + V\frac{\partial U}{\partial Y}\right) + \frac{U}{Da\sqrt{(Ra/Pr)}} = -\frac{\partial P}{\partial X} + \frac{B}{\sqrt{(Ra/Pr)}}\left(\frac{\partial^2 U}{\partial X^2} + \frac{\partial^2 U}{\partial Y^2}\right) - \frac{C}{\sqrt{Da}}|U|U \tag{6}$$

$$A\left(U\frac{\partial V}{\partial X} + V\frac{\partial V}{\partial Y}\right) + \frac{V}{Da\sqrt{(Ra/Pr)}} = -\frac{\partial P}{\partial Y} + \frac{B}{\sqrt{(Ra/Pr)}}\left(\frac{\partial^2 V}{\partial X^2} + \frac{\partial^2 V}{\partial Y^2}\right) - \frac{C}{\sqrt{Da}}|U|V + \theta \tag{7}$$

$$U\frac{\partial \theta}{\partial X} + V\frac{\partial \theta}{\partial Y} = \frac{1}{\sqrt{(RaPr)}}\left(\frac{\partial^2 \theta}{\partial X^2} + \frac{\partial^2 \theta}{\partial Y^2}\right) \tag{8}$$

where $|U| = \sqrt{(U^2 + V^2)}$.

The following dimensionless parameters appear in the governing equations:

$Ra = g\beta\Delta TL^3/(\nu\alpha)$ Rayleigh number

$Pr = \nu/\alpha$ Prandtl number

$Da = \dfrac{K}{L^2}$ Darcy number

ν and α are the kinematic viscosity and the thermal diffusivity of the fluid medium, respectively. In addition to the above mentioned dimensionless parameters, a Darcy-modified Rayleigh number is defined as $Ra^* = Ra \times Da$.

Equations (5)–(8) are subjected to the following hydrodynamic boundary conditions:

Model I	Models II, III and IV		
$U = 0$	$U = 0, V = 0$	at $X = 0, 1$	$0 \leqslant Y \leqslant 1$
$V = 0$	$U = 0, V = 0$	at $Y = 0, 1$	$0 \leqslant X \leqslant 1$

For Model I, only the impermeable boundary condition is specified whereas for Models II, III and IV, the no-slip and impermeable boundary conditions are prescribed.

The thermal boundary conditions are as follows:

$\theta = 0$	at $X = 0$	$0 \leqslant Y \leqslant 1$
$\theta = 1$	at $X = 1$	$0 \leqslant Y \leqslant 1$
$\dfrac{\partial \theta}{\partial Y} = 0$	at $Y = 0, 1$	$0 < X < 1$

Solution procedure

The set of equations (5)–(8) is discretized by employing the conventional Galerkin scheme. The nonlinearities are treated by the Newton-Raphson method[23] and the resulting system of linear equations are solved by a Frontal solver. An eight-noded isoparametric element is used

for discretization of the solution domain. A quadratic shape function is used for interpolation of velocity and temperature fields, while a linear shape function is assumed for interpolation of pressure. Once a solution is obtained to the set of equations (5)–(8), the stream function solution is obtained as a part of post-processing operation. The solution for the stream function is obtained from the following equation:

$$\frac{\partial^2 \Psi}{\partial X^2} + \frac{\partial^2 \Psi}{\partial Y^2} = -\Omega \tag{9}$$

with $\Psi = 0$ on all the bounding surfaces ($X = 0, 1$ and $Y = 0, 1$) where Ψ is the nondimensional stream function defined as:

$$U = \frac{\partial \Psi}{\partial Y}, \qquad V = -\frac{\partial \Psi}{\partial X} \tag{10}$$

and Ω is the nondimensional vorticity, defined as:

$$\Omega = \left(\frac{\partial V}{\partial X} - \frac{\partial U}{\partial Y}\right) \tag{11}$$

Distribution of the Nusselt number along the cold and hot walls are defined as:

$$\overline{Nu}_{c,h} = \left.\frac{\partial \theta}{\partial X}\right|_{X = 0,1} \tag{12}$$

and the average Nusselt number is calculated as:

$$\overline{Nu}_{c,h} = \int_0^1 Nu_{c,h}\, dY \tag{13}$$

where subscripts c and h denote cold and hot wall quantities respectively.

Grid independence study and convergence criteria

The grid independence study has been carried out with $Ra = 10^8$ and $Da = 10^{-5}$. The study has been started with a nonuniform mesh of 14×14 elements along both the x and y directions. Subsequently, refined meshes have been considered with 18×14, 22×14, 26×14 and 22×18 elements in the x and y directions, respectively. Since the front-width increases with the increase of element numbers in both the coordinate directions, a mesh of 22×14 has been finally adopted for all the subsequent studies. A greater refinement of the mesh has been considered in the x direction, along which the thermal gradient is steeper. To resolve the sharp velocity and temperature gradients near the boundaries, finer meshes have been adopted near the solid walls. The study has been performed, individually, for all the models considering the variations of such quantities as maximum U and V velocities, ψ_{max}, $\overline{Nu}$ etc. However, for the sake of brevity, only ψ_{max} and $\overline{Nu}$ are presented in *Table 1*.

For the convergence criteria, the limits of relative change of any variable and the weighted nodal residue are taken as 10^{-4} and 10^{-8} respectively for Models I, II and III and the same are set to 10^{-3} and 10^{-6}, respectively, for Model IV. A less stringent convergence criteria is set for Model IV because of its relatively slower convergence pattern compared to the other models considered. Furthermore, the centro-symmetric nature of the flow and the overall energy balance on the hot and the cold walls are considered as criteria of additional checks for each of the cases reported in the present study.

Table 1 Results of grid independence study

A. Darcy Model (Ra = 10^8, Da = 10^{-5})

Grid size	$\Psi_{max} \times 10^2$ (X, Y)	$\overline{Nu}$
14 × 14	0.244 (0.690, 0.440)	14.102
18 × 14	0.245 (0.214, 0.560)	14.010
22 × 14	0.243 (0.214, 0.560)	13.954
26 × 14	0.243 (0.242, 0.560)	13.952
22 × 18	0.243 (0.214, 0.554)	13.904

B. Brinkman-extended Darcy Model (Ra = 10^8, Da = 10^{-5})

Grid size	$\Psi_{max} \times 10^2$ (X, Y)	$\overline{Nu}$
14 × 14	0.225 (0.690, 0.440)	12.487
18 × 14	0.225 (0.786, 0.440)	12.458
22 × 14	0.223 (0.690, 0.440)	12.408
26 × 14	0.223 (0.758, 0.440)	12.407
22 × 18	0.223 (0.690, 0.446)	12.375

C. Brinkman-extended Darcy Model with convective terms (Ra = 10^8, Da = 10^{-5})

Grid size	$\Psi_{max} \times 10^2$ (X, Y)	$\overline{Nu}$
14 × 14	0.224 (0.690, 0.440)	12.482
18 × 14	0.224 (0.786, 0.440)	12.455
22 × 14	0.222 (0.690, 0.440)	12.406
26 × 14	0.222 (0.758, 0.440)	12.404
22 × 18	0.222 (0.690, 0.446)	12.373

D. Brinkman-Forchheimer-extended Darcy Model (Ra = 10^8, Da = 10^{-5})

Grid size	$\Psi_{max} \times 10^2$ (X, Y)	$\overline{Nu}$
14 × 14	0.189 (0.690, 0.440)	10.386
18 × 14	0.188 (0.437, 0.500)	10.358
22 × 14	0.189 (0.690, 0.440)	10.296
26 × 14	0.189 (0.694, 0.440)	10.296
22 × 18	0.189 (0.690, 0.446)	10.267

Validation of the code

For the purpose of validation of the code and checking the accuracy of the results, a comparison of the overall Nusselt number is made with some of the available works. The overall agreement is found to be quite satisfactory. Details of this comparison is furnished in *Table 2*.

RESULTS AND DISCUSSION

In the present study the following range of parameters is considered:

$$Ra^* = 50, 100, 200, 500, 1000$$

Each of the above Ra^* is obtained by considering $Ra = 10^5, 10^6, 10^7, 10^8$ and corresponding values of Da are considered. The Prandtl number, Pr, of the fluid is consistently taken as 0.71 except for the purpose of comparison of Model IV in *Table 2*.

With the above-mentioned set of parameter combinations, analysis is performed with each of the models to study the flow structure and heat transfer characteristics in each case. In order to emphasize the variation between the four models, the extreme values of Ra^* and Da have been considered which are expected to highlight the important aspects, particularly the near wall behaviour.

Table 2   Comparison of average Nusselt number $(\overline{Nu})$

A. Darcy formulation (Model I)

Ra^*	Present work	Walker and Homsy[2]	Shiralkar et al.[4]	Ni and Beckermann[6]	Bejan[8]	Beckermann et al.[12]
50	1.988	1.98			1.897	1.981
100	3.125	3.097	3.115	3.013	3.433	3.113
200	5.016	4.89	4.976		6.044	5.038
500	9.132	8.66	8.944	8.892		9.308
1000	13.954	12.96	13.534	13.42		

B. Brinkman-extended Darcy formulation (Model II)

Ra^*	Da	Present work	Lauriat and Prasad[10]
100	10^{-3}	2.425	2.41
	10^{-4}	2.857	2.84
	10^{-5}	3.034	3.02
	10^{-6}	3.094	3.06
1000	10^{-2}	4.262	4.26
	10^{-3}	7.208	7.29
	10^{-4}	10.278	10.34
	10^{-5}	12.408	12.42

C. Brinkman-Forchheimer-extended Darcy formulation (Model IV)

Ra^*	Da	Pr	Present work	Beckermann et al.[12]
10^4	10^{-1}	1.0	4.357	4.385

Vertical velocity at cavity mid-height

The vertical velocity (V) distributions at cavity mid-height $(Y = 0.5)$ are shown in *Figure 2(a)–(d)*. *Figure 2(a)* corresponds to $Ra^* = 50$ $(Ra = 10^8, Da = 5 \times 10^{-7})$. In this figure all the curves are found to merge with each other except in the vicinity of the wall. However, for Models II, III and IV the maximum velocity is attained at a location very close to the wall. *Figure 2(b)* corresponds to the same value of $Ra^* = 50$ with a different Rayleigh and Darcy number combination $(Ra = 10^5, Da = 5 \times 10^{-4})$. In this case the deviation between the models are more prominent compared to the case presented in *Figure 2(a)*. Moreover, the location of the peak velocity is found to shift away from the wall as the Da value is increased. *Figures 2(c)* and *2(d)* correspond to the value of $Ra^* = 1000$. The disagreement between the different models is evident in both cases, with the deviation being more prominent in *Figure 2(d)* than in *Figure 2(c)*. Unlike *Figures 2(a)* and *2(b)*, where the flow is found to occur throughout the cavity, stagnation in the core is evident from the velocity distributions in *Figures 2(c)* and *2(d)*.

For any fixed value of Ra^*, the velocity distribution for Model I remains similar. However, due to the Rayleigh number dependent way of velocity scaling, the non-dimensional velocity is reduced by a factor of $\sqrt{Ra}$. Hence the magnitudes are different between *Figures 2(a)* and *2(b)* and between *Figures 2(c)* and *2(d)*. For all the cases, Model II and Model III practically overlap with each other, with negligible difference visible in *Figure 2(d)* corresponding to the highest Darcy number $(Da = 10^{-2})$ considered in the present work. The magnitude of the maximum velocity is highest for Model I. Comparatively the magnitude of the maximum velocity is smaller for Models II and III due to the introduction of the frictional term. In the case of Model IV, the magnitude of the maximum velocity is still smaller due to the incorporation of the inertia term. With regards to the location of the maximum velocity, it occurs exactly on the solid wall for Model I where only the impermeable boundary condition is prescribed. However, for Model IV, the location is nearer to the wall than those for Models II and III.
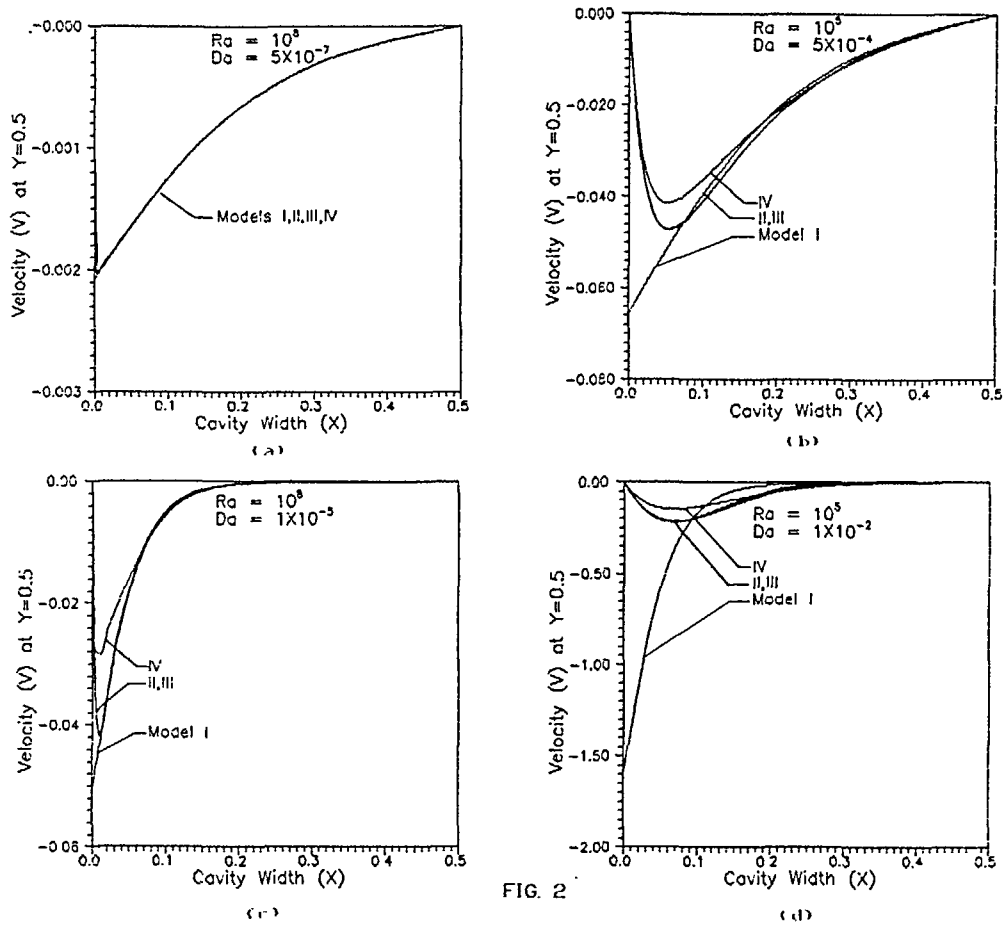
Figure 2 Velocity (V) distribution at cavity mid-height $(Y = 0.5)$: (a) $Ra = 10^8$ and $Da = 5 \times 10^{-7}$; (b) $Ra = 10^5$ and $Da = 5 \times 10^{-4}$; (c) $Ra = 10^8$ and $Da = 10^{-5}$; (d) $Ra = 10^5$ and $Da = 10^{-2}$

Temperature distribution at cavity mid-height

The temperature distributions at cavity mid-height $(Y = 0.5)$ are shown in *Figures 3(a)–(d)*. *Figures 3(a)* and *3(b)* correspond to $Ra^* = 50$ where all models virtually coincide with each other. The temperature distributions in these two cases $(Ra = 10^8, Da = 5 \times 10^{-7}$ and $Ra = 10^5$, $Da = 5 \times 10^{-4})$ are identical because the flow is Darcian in nature and the flow structure and heat transfer are uniquely governed by the value of Ra^*. The more or less linear variation of temperature indicates that the transport is conduction dominated. The effects of convection and core stratification are evident in *Figures 3(c)* and *3(d)* corresponding to $Ra^* = 1000$. Again for *Figure 3(c)*, the temperature distribution for Models II, III and IV are found to collapse on that for Model I. In *Figure 3(d)*, the effects of the Brinkman extension and the Forchheimer extension are clearly evident. In all these cases, Models II and III show an identical distribution indicating that the contribution of the transport term in Model III is negligible. However, with the introduction of the frictional terms, the flow is retarded when compared to that in Model I. This in turn causes a reduction in heat transfer compared to the Darcian flow model. Furthermore, with the introduction of the inertia term in Model IV, the flow is further arrested
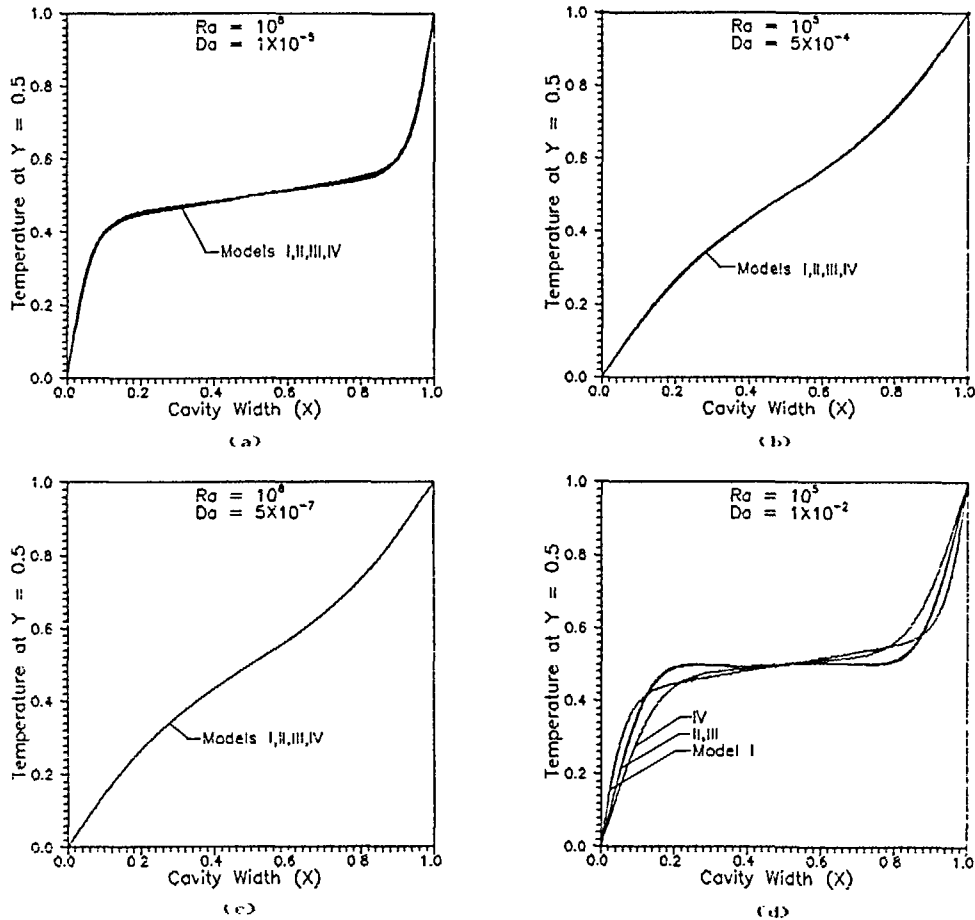
Figure 3 Temperature (θ) distribution at cavity mid-height ($Y = 0.5$): (a) $Ra = 10^8$ and $Da = 5 \times 10^{-7}$; (b) $Ra = 10^5$ and $Da = 5 \times 10^{-4}$; (c) $Ra = 10^8$ and $Da = 10^{-5}$; (d) $Ra = 10^5$ and $Da = 10^{-2}$

causing further reduction in heat transfer. This is corroborated in *Figure 3(d)*. Model I indicates the steepest temperature gradient near the wall and Model IV indicates the lowest value of near wall temperature gradient while Models II and III lie in between Model I and Model IV.

Streamfunction and isotherm contours

The flow patterns and isotherm contours are presented in *Figures 4(a)–4(d)* and *Figures 5(a)–5(d)*. In both of these sets of figures, the modified Rayleigh number Ra^* is taken as 1000. The strength of circulation in each case is indicated by the value of ψ_{max}. The magnitude and the location of ψ_{max} are presented in each figure. The physical boundary of the problem domain is set to the value of $\psi = 0.0$. The other stream function contours are equally spaced between the values of ψ_{max} and $\psi = 0.0$.

Figures 4(a)–4(d) correspond to Models I, II, III and IV. $Ra = 10^8$ and $Da = 10^{-5}$ are considered in these cases. From these figures, it is evident that the overall nature of the streamlines are similar to each other for all the models. The flow patterns obtained are typical of the Darcian flow regime. Due to the small value of Da, all models tend to behave like the Darcy flow model.

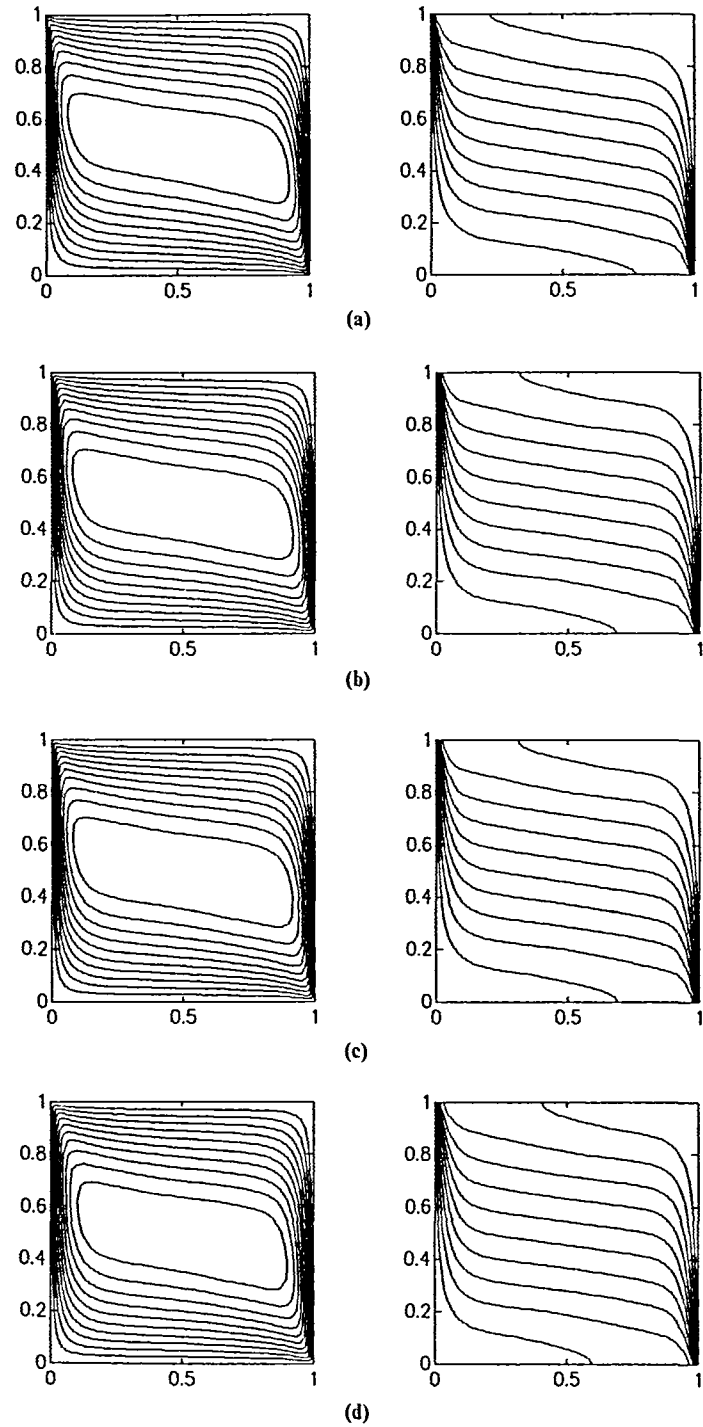*Figure 4* Stream function and isotherm contours for $Ra = 10^8$ and $Da = 10^{-5}$: (a) Model I, $\psi_{max}(X, Y) = 0.243 \times 10^{-2}$ (0.214, 0.560); (b) Model II, $\psi_{max}(X, Y) = 0.223 \times 10^{-2}$ (0.690, 0.440); (c) Model III, $\psi_{max}(X, Y) = 0.222 \times 10^{-2}$ (0.690, 0.440); (d) Model IV, $\psi_{max}(X, Y) = 0.189 \times 10^{-2}$ (0.690, 0.440)

The Darcian flow is characterized by the occurrence of the maximum vertical velocity exactly on the vertical solid wall. Moreover, a velocity boundary layer is set up in the lower part of the hot wall. In the upper part of the hot wall, the flow tends to bend towards the top of the cold wall, following the upper horizontal wall. Along the cold wall, a similar type of boundary layer develops from the upper part of this wall. In the lower part of the cold wall, the flow bends toward the bottom part of hot wall along the lower adiabatic wall to make up the void created by the buoyant fluid at the bottom of the hot wall. In this way, the circulation is established in the cavity. The axis of the streamlines is oriented along a line, inclined upward from the hot to the cold wall. With the introduction of the friction terms in Model II and incorporation of the no-slip boundary condition, the position of the peak velocity shifts away from the solid wall. But it still occurs at a location very close to the vertical walls, as seen from *Figure 2(c)*. However, due to the frictional effect, introduced by the momentum diffusion terms, the magnitude of the peak velocity decreases in comparison to the Darcy model. This results in a slight thickening of the boundary layer as observed in *Figure 4(b)*. The incorporation of the convection terms in Model III does not significantly affect the flow patterns in *Figure 4(c)* at this low value of Darcy number $(Da = 10^{-5})$. In Model IV, due to the simultaneous presence of the friction and inertia terms, the flow is further retarded. This is evident from the increased spacings between the streamlines, as seen in *Figure 4(d)*. The gradual decrease in the strength of circulation for Models II, III and IV due to the friction, convection and inertia terms is corroborated by the decreasing values of ψ_{max}, shown alongside *Figures 4(b)* to *4(d)* respectively, compared to the value of ψ_{max} in *Figure 4(a)* for Model I.

The isotherm contours are also presented alongside the streamline patterns in *Figures 4(a)-(d)* for the different models with $Ra = 10^8$ and $Da = 10^{-5}$. The overall nature of the isotherms in *Figures 4(b)-4(d)*, corresponding to Models II, III and IV, are quite similar to the isotherms in *Figure 4(a)* for Model I. The isotherms in *Figure 4(a)* are typical of the Darcy flow model. Moreover, since the Darcy number is small $(Da = 10^{-5})$, the flow is Darcian in nature. Thus, the flow, and, consequently, the isotherm patterns for Models II, III and IV agree closely with those of Model I. However, a close inspection of the isotherms in these figures reveal a slight increase in spacings between isotherms, particularly at the top and bottom corners of the cold and hot walls respectively, for Models II, III and IV compared to those for Model I. This rarefaction of isotherm spacings in Models II, III and IV over those in Model I can be attributed to the gradual decrease of the flow intensity in Models II, III and IV compared to that in Model I. With the decrease in intensity of flow, the overall rate of heat transfer diminishes which is reflected in the slight rarefaction of isotherm spacings gradually in *Figures 4(a)-4(d)*.

The stream function and isotherm contours are presented in *Figures 5(a)-5(d)*, corresponding to Models I, II, III and IV, for $Ra = 10^5$ and $Da = 10^{-2}$. The large value of Darcy number is considered to highlight the distinctive features of the models. *Figure 5(a)* shows the streamlines for the Darcy model. For the Darcy model, the flow pattern is solely determined by the value of Ra^*, rather than the values of Ra and Da. This is evident from the identical streamline patterns shown in *Figures 4(a)* and *5(a)*. *Figure 5(b)* corresponds to the Brinkman-extended Darcy model. Due to the frictional effects, incorporated in Model II, the flow slows down considerably. This is distinctly evident from the values of ψ_{max}, for the large value of Da, in *Figure 5(b)* as compared to the same in *Figure 5(a)*. For $Ra^* = 1000$ and $Da = 10^{-2}$, the flow pattern tends to approach that of a buoyancy induced flow in absence of a porous medium when Model III is considered. In this case, due to the incorporation of the convection terms, the buoyant fluid moves upward along the hot wall and impinges on the top wall. The fluid then suffers a reflection and moves towards the cold wall. The heated fluid, as it comes in contact with the cold wall, gets heavier and moves down the cold wall. The fluid then strikes the bottom adiabatic wall with a high velocity and another hydraulic jump occurs. Then, it moves rapidly horizontally towards the hot wall to make up the void at the base of the hot wall. In this way, the circulation is established in the cavity. One of the distinctive features of this model is that, in this case, the axis of the circulation is tilted downward from the hot to the cold wall. This

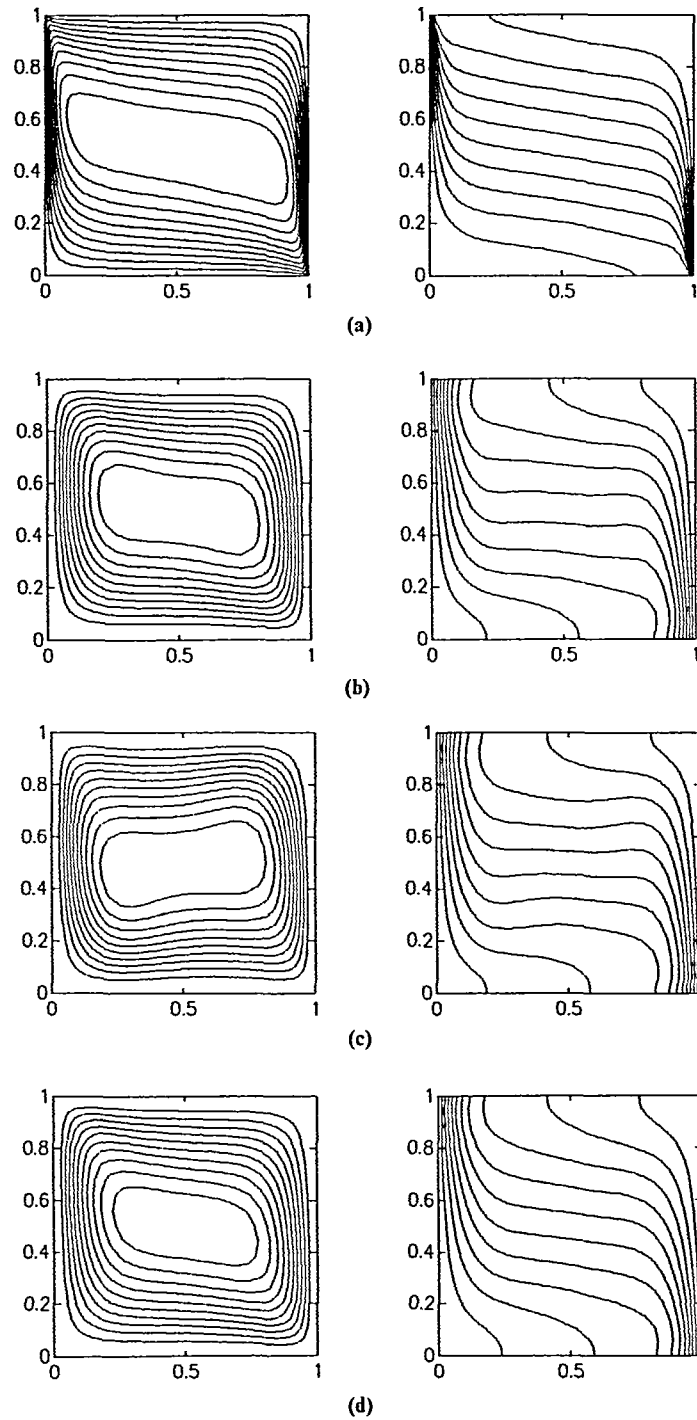*Figure 5* Stream function and isotherm contours for $Ra = 10^5$ and $Da = 10^{-2}$: (a) Model I, $\psi_{max}(X, Y) = 0.769 \times 10^{-1}$ (0.214, 0.560); (b) Model II, $\psi_{max}(X, Y) = 0.325 \times 10^{-1}$ (0.690, 0.440); (c) Model III, $\psi_{max}(X, Y) = 0.305 \times 10^{-1}$ (0.309, 0.440); (d) Model IV, $\psi_{max}(X, Y) = 0.255 \times 10^{-1}$ (0.548, 0.500)

reversal of the direction of the tilt of the circulation is due to the occurrence of the couple of hydraulic jumps near the top-right and bottom-left corners of the cavity. The flow pattern for Model IV, as seen from *Figure 5(d)*, is one of a heavily retarded flow caused by the inertia effect of the Forchheimer extension. Besides, due to the presence of the momentum diffusion terms, in Models II, III and IV, the circulation penetrates deeper towards the centre of the cavity. This is in contrast to Model I. For Model I, in absence of the restrictive effects imposed by the inertia term, the flow intensity is large. Moreover, due to the absence of the momentum diffusion terms, the high velocity flow, remains largely restricted near the active walls of the cavity. A large part in the central portion of the cavity experiences a very weak circulation.

A brief discussion on the isotherms shown alongside the streamlines is in order for the different models in *Figures 5(a)–5(d)* for $Ra = 10^5$ and $Da = 10^{-2}$. The isotherms for Model I, shown in *Figure 5(a)* are exactly similar to those shown in *Figure 4(a)* for $Ra = 10^8$ and $Da = 10^{-5}$. This is expected because of the same value of modified Rayleigh number ($Ra^* = 1000$) in these two cases, which determines the flow and heat transfer in the Darcy flow model. With the introduction of viscous diffusion terms and incorporation of no-slip boundary conditions in the Brinkman-extended Darcy model, the flow intensity is largely reduced. This results in a sharp decrease in heat transfer rate. The drop in heat transfer rate is manifested through wider spacings between isotherms in *Figure 5(b)* compared to those for the Darcy model as shown in *Figure 5(a)*. Furthermore, in Model III, due to the incorporation of transport terms, coupled with a large value of $Da = 10^{-2}$, the flow approaches the buoyancy driven flow of a free fluid. As a result, the isotherms are similar to those observed in a differentially heated vertical square cavity. In Model IV, the inertia terms of the Forchheimer-extension causes further retardation of the flow. This results in further decrease in heat transfer rate. This is evident from the increase in spacings between isotherms compared to all other models.

Nusselt number distribution on cold wall

The Nusselt number distribution on the cold wall are shown in *Figure 6(a)–6(d)*. Figures 6(a) and 6(b) correspond to $Ra^* = 50$, while *Figures 6(c)* and 6(d) correspond to $Ra^* = 1000$. In *Figure 6(a)*, the flow is found to be fully Darcian due to the very low value of $Da = 5 \times 10^{-7}$, where all models practically coincide with each other. In *Figure 6(b)*, deviation of the non-Darcian models (Models II, III and IV) from the Darcian flow model (Model I) is evident due to the increased value of Da. The non-Darcian models are found to predict lower values of the Nusselt number compared to the Darcian model for any given value of Ra^*. The reasons are explained during the discussion on temperature distribution at cavity mid-height. In *Figure 6(d)*, the deviation between Model I and Model II, III and IV reaches a maximum due to the large value of $Da = 1 \times 10^{-2}$.

The Nusselt number distribution shows an identical pattern, as long as Ra^* remains constant, for Model I. However, for other models, this distribution depends exclusively on the value of Ra and Da. For all cases, Models II and III show identical distributions indicating the negligible contribution of the transport terms. For any value of Ra^*, Model I predicts the highest value of $\overline{Nu}$ and Model IV predicts the lowest value of $\overline{Nu}$, while the Models II and III predictions in between.

Overall Nusselt number $(\overline{Nu})$ and maximum stream function (Ψ_{max})

The overall Nusselt number and maximum stream function together with its location are given in *Tables 3–7* for different modified Rayleigh numbers (Ra^*).

At any fixed Ra^*, the $\overline{Nu}$ is found to be independent of Ra and Da combinations for Model I. However, for the Rayleigh number dependent way of velocity scaling, the magnitude of Ψ_{max}
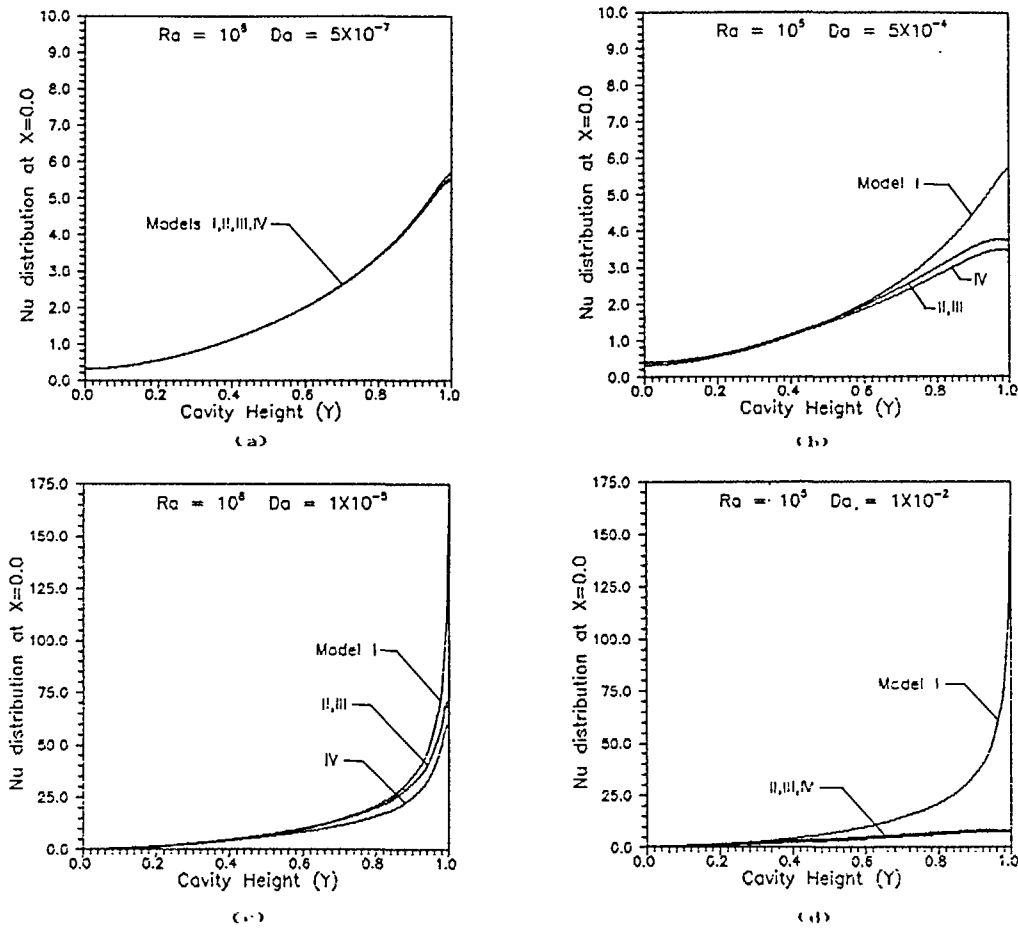
Figure 6 Nusselt number (*Nu*) distribution on the cold wall ($X = 0.0$): (a) $Ra = 10^8$ and $Da = 5 \times 10^{-7}$; (b) $Ra = 10^5$ and $Da = 5 \times 10^{-4}$; (c) $Ra = 10^8$ and $Da = 10^{-5}$; (d) $Ra = 10^5$ and $Da = 10^{-2}$

Table 3 Average Nusselt number ($\overline{Nu}$) and maximum stream function (Ψ_{max}) at $Ra^* = 50$

Da		Model I	Model II	Model III	Model IV
5×10^{-4}	$\overline{Nu}$	1.988	1.765	1.765	1.667
	Ψ_{max}	0.107×10^{-1}	0.967×10^{-2}	0.967×10^{-2}	0.899×10^{-2}
	(X, Y)	(0.500, 0.500)	(0.500, 0.500)	(0.500, 0.500)	(0.500, 0.500)
5×10^{-5}	$\overline{Nu}$	1.988	1.911	1.911	1.858
	Ψ_{max}	0.338×10^{-2}	0.328×10^{-2}	0.328×10^{-2}	0.318×10^{-2}
	(X, Y)	(0.500, 0.500)	(0.500, 0.500)	(0.500, 0.500)	(0.500, 0.500)
5×10^{-6}	$\overline{Nu}$	1.988	1.963	1.963	1.942
	Ψ_{max}	0.107×10^{-2}	0.106×10^{-2}	0.106×10^{-2}	0.105×10^{-2}
	(X, Y)	(0.500, 0.500)	(0.500, 0.500)	(0.500, 0.500)	(0.500, 0.500)
5×10^{-7}	$\overline{Nu}$	1.988	1.979	1.979	1.971
	Ψ_{max}	0.338×10^{-3}	0.338×10^{-3}	0.338×10^{-3}	0.337×10^{-3}
	(X, Y)	(0.500, 0.500)	(0.500, 0.500)	(0.500, 0.500)	(0.500, 0.500)

D. MISRA AND A. SARKAR

Table 4 Average Nusselt number $(\overline{Nu})$ and maximum stream function (Ψ_{max}) at $Ra^* = 100$

Da		Model I	Model II	Model III	Model IV
10^{-3}	$\overline{Nu}$	3.125	2.425	2.425	2.164
	Ψ_{max}	0.177×10^{-1}	0.147×10^{-1}	0.147×10^{-1}	0.130×10^{-1}
	(X, Y)	(0.500, 0.500)	(0.500, 0.500)	(0.500, 0.500)	(0.500, 0.500)
10^{-4}	$\overline{Nu}$	3.125	2.857	2.857	2.657
	Ψ_{max}	0.559×10^{-2}	0.524×10^{-2}	0.524×10^{-2}	0.490×10^{-2}
	(X, Y)	(0.500, 0.500)	(0.500, 0.500)	(0.500, 0.500)	(0.500, 0.500)
10^{-5}	$\overline{Nu}$	3.125	3.034	3.034	2.938
	Ψ_{max}	0.177×10^{-2}	0.173×10^{-2}	0.173×10^{-2}	0.168×10^{-2}
	(X, Y)	(0.500, 0.500)	(0.500, 0.500)	(0.500, 0.500)	(0.500, 0.500)
10^{-6}	$\overline{Nu}$	3.125	3.094	3.094	3.057
	Ψ_{max}	0.559×10^{-3}	0.557×10^{-3}	0.557×10^{-3}	0.551×10^{-3}
	(X, Y)	(0.500, 0.500)	(0.500, 0.500)	(0.500, 0.500)	(0.500, 0.500)

Table 5 Average Nusselt number $(\overline{Nu})$ and maximum stream function (Ψ_{max}) at $Ra^* = 200$

Da		Model I	Model II	Model III	Model IV
2×10^{-3}	$\overline{Nu}$	5.016	3.144	3.136	2.676
	Ψ_{max}	0.283×10^{-1}	0.204×10^{-1}	0.202×10^{-1}	0.172×10^{-1}
	(X, Y)	(0.548, 0.500)	(0.500, 0.500)	(0.500, 0.500)	(0.500, 0.500)
2×10^{-4}	$\overline{Nu}$	5.016	4.160	4.158	3.626
	Ψ_{max}	0.896×10^{-2}	0.785×10^{-2}	0.783×10^{-2}	0.694×10^{-2}
	(X, Y)	(0.548, 0.500)	(0.500, 0.500)	(0.500, 0.500)	(0.500, 0.500)
2×10^{-5}	$\overline{Nu}$	5.016	4.697	4.697	4.342
	Ψ_{max}	0.283×10^{-2}	0.271×10^{-2}	0.270×10^{-2}	0.253×10^{-2}
	(X, Y)	(0.548, 0.500)	(0.500, 0.500)	(0.500, 0.500)	(0.500, 0.500)
2×10^{-6}	$\overline{Nu}$	5.016	4.908	4.908	4.745
	Ψ_{max}	0.896×10^{-3}	0.885×10^{-3}	0.885×10^{-3}	0.860×10^{-3}
	(X, Y)	(0.548, 0.500)	(0.548, 0.500)	(0.548, 0.500)	(0.548, 0.500)

Table 6 Average Nusselt number $(\overline{Nu})$ and maximum stream function (Ψ_{max}) at $Ra^* = 500$

Da		Model I	Model II	Model III	Model IV
5×10^{-3}	$\overline{Nu}$	9.132	3.903	3.858	3.249
	Ψ_{max}	0.509×10^{-1}	0.277×10^{-1}	0.268×10^{-1}	0.222×10^{-1}
	(X, Y)	(0.690, 0.440)	(0.595, 0.500)	(0.309, 0.500)	(0.500, 0.500)
5×10^{-4}	$\overline{Nu}$	9.132	6.030	6.004	4.870
	Ψ_{max}	0.161×10^{-1}	0.119×10^{-1}	0.117×10^{-1}	0.969×10^{-2}
	(X, Y)	(0.690, 0.440)	(0.500, 0.500)	(0.548, 0.500)	(0.548, 0.500)
5×10^{-5}	$\overline{Nu}$	9.132	7.720	7.711	6.477
	Ψ_{max}	0.509×10^{-2}	0.450×10^{-2}	0.448×10^{-2}	0.385×10^{-2}
	(X, Y)	(0.690, 0.440)	(0.500, 0.500)	(0.500, 0.500)	(0.548, 0.500)
5×10^{-6}	$\overline{Nu}$	9.132	8.612	8.612	7.772
	Ψ_{max}	0.161×10^{-2}	0.154×10^{-2}	0.154×10^{-2}	0.141×10^{-2}
	(X, Y)	(0.690, 0.440)	(0.690, 0.440)	(0.690, 0.440)	(0.690, 0.440)

Table 7   Average Nusselt number $(\overline{Nu})$ and maximum stream function (Ψ_{max}) at $Ra^* = 1000$

Da		Model I	Model II	Model III	Model IV
10^{-2}	$\overline{Nu}$	13.954	4.262	4.176	3.585
	Ψ_{max}	0.769×10^{-1}	0.325×10^{-1}	0.305×10^{-1}	0.255×10^{-1}
	(X, Y)	(0.214, 0.560)	(0.690, 0.440)	(0.309, 0.440)	(0.548, 0.500)
10^{-3}	$\overline{Nu}$	13.954	7.208	7.136	5.666
	Ψ_{max}	0.243×10^{-1}	0.149×10^{-1}	0.145×10^{-1}	0.116×10^{-1}
	(X, Y)	(0.214, 0.560)	(0.214, 0.560)	(0.214, 0.500)	(0.548, 0.500)
10^{-4}	$\overline{Nu}$	13.954	10.278	10.236	8.012
	Ψ_{max}	0.769×10^{-2}	0.613×10^{-2}	0.607×10^{-2}	0.486×10^{-2}
	(X, Y)	(0.214, 0.560)	(0.214, 0.560)	(0.214, 0.560)	(0.690, 0.440)
10^{-5}	$\overline{Nu}$	13.954	12.408	12.406	10.296
	Ψ_{max}	0.243×10^{-2}	0.223×10^{-2}	0.222×10^{-2}	0.189×10^{-2}
	(X, Y)	(0.214, 0.560)	(0.690, 0.440)	(0.690, 0.440)	(0.690, 0.440)

decreases with increasing Ra. At any fixed Ra^*, Model I predicts the highest value of $\overline{Nu}$ and Ψ_{max}. However, with the introduction of the viscous terms in Models II and III, and consequent incorporation of the no-slip boundary condition, the strength of the flow weakens and a fall in the $\overline{Nu}$ is observed. This fall is pronounced for high values of Da. For all practical purposes, Models II and III predict identical values of $\overline{Nu}$ and Ψ_{max}. However a slight decrement of $\overline{Nu}$ and Ψ_{max} are observed for Model III when Da is large. In Model IV, a further reduction in $\overline{Nu}$ and Ψ_{max} are evident due to the incorporation of the inertia term. The agreement between the different models are closer for low values of Ra^* and Da and the divergence between them becomes pronounced for high values of Ra^* and Da.

CONCLUSIONS

A finite element analysis is performed for comparison of alternative models for natural convection in a differentially heated square cavity filled with fluid saturated porous media in the range of $50 \leqslant Ra^* \leqslant 1000$, $5 \times 10^{-7} \leqslant Da \leqslant 10^{-2}$. Comparison with existing results reveal satisfactory agreement with the results obtained from the present analysis.

From a comparison of velocity, temperature and heat flux distributions obtained from the different porous models, the following conclusions are drawn:

(i) For low values of Ra^* and Da, all models practically merge with the Darcy flow model;

(ii) For the Darcy flow model Ra^* exclusively governs the flow structure and heat transfer. However, for the Brinkman-Forchheimer-extended Darcy flow models, individual values of Ra and Da are the influencing parameters.

(iii) For the range of Da considered in the present study, the contribution of the transport terms in Model III are negligible such that Models II and III predict identical results. However, for high values of Da, a slight reduction of flow strength and heat transfer is caused by the transport terms of Model III.

(iv) For a given value of Ra^*, the Darcy flow model predicts the highest maximum velocity at the cavity mid-height and overall heat transfer rate. For the Darcy flow model, the maximum velocity occurs exactly on the solid wall. On the other hand, the Brinkman-Forchheimer-extended Darcy equations predict the weakest velocity field and lowest heat transfer rate. For the Brinkman-extended models (Models II and III) these values lie in between those of Models I and IV.

REFERENCES

1 Cheng, P. *Heat Transfer in Geothermal Systems, Advances in Heat Transfer*, Academic Press, New York, **14**, 1–105 (1978)
2 Walker, K. L. and Homsy, G. M. Convection in a porous cavity, *J. Fluid Mech.*, **87**, 449–474 (1978)
3 Hickox, C. E. and Gartling, D. K. A numerical study of natural convection in a porous layer subjected to an end-to-end temperature difference, *Trans. ASME J. Heat Transfer*, **103**, 797–802 (1981)
4 Shiralkar, G. S., Haajizadeh, M. and Tien, C. L. Numerical study of high Rayleigh number convection in a vertical porous enclosure, *Numer. Heat Transfer*, **6**, 223–234 (1983)
5 Prasad, V. and Kulacki, F. A. Convective heat transfer in a rectangular porous cavity – effect of aspect ratio on flow structure and heat transfer, *Trans. ASME J. Heat Transfer*, **106**, 158–165 (1984)
6 Ni, J. and Beckermann, C. Natural convection in a vertical enclosure filled with anisotropic porous media, *Trans. ASME J. Heat Transfer*, **113**, 1033–1037 (1991)
7 Burns, P. J., Chow, L. C. and Tien, C. L. Convection in a vertical slot filled with porous insulation, *Int. J. Heat Mass Transfer*, **20**, 919–926 (1977)
8 Bejan, A. Natural convection heat transfer in a porous layer with internal flow obstructions, *Int. J. Heat Mass Transfer*, **26**, 815–822 (1983)
9 Chan, B. K. C., Ivey, C. M. and Barry, J. M. Natural convection in enclosed porous media with rectangular boundaries, *Trans. ASME J. Heat Transfer*, **92**, 21–27 (1970)
10 Lauriat, G. and Prasad, V. Natural convection in a vertical porous cavity: A numerical study for Brinkman-extended Darcy formulation, *Trans. ASME J. Heat Transfer*, **109**, 688–696 (1987)
11 Prasad, V. and Tuntomo, A. Inertial effects on natural convection in a vertical porous cavity, *Numer. Heat Transfer*, **11**, 295–320 (1987)
12 Beckermann, C., Viskanta, R. and Ramadhyani, S. A numerical study of non-Darcian natural convection in a vertical enclosure filled with a porous medium, *Numer. Heat Transfer*, **10**, 557–570 (1986)
13 Lauriat, G. and Prasad, V. Non-Darcian effects on natural convection in a vertical porous enclosure, *Int. J. Heat Mass Transfer*, **32**, 2135–2148 (1989)
14 Poulikakos, D. and Bejan, A. Natural convection in vertically and horizontally layered porous media heated from the side, *Int. J. Heat Mass Transfer*, **26**, 1805–1814 (1983)
15 Lai, F. C. and Kulacki, F. A. Natural convection across a vertical layered porous cavity, *Int. J. Heat Mass Transfer*, **31**, 1247–1260 (1988)
16 Beckermann, C., Ramadhyani, S. and Viskanta, R. Natural convection flow and heat transfer between a fluid layer and a porous layer inside a rectangular enclosure, *Trans. ASME J. Heat Transfer*, **109**, 363–370 (1987)
17 Beckermann, C., Viskanta, R. and Ramadhyani, S. Natural convection in vertical enclosures containing simultaneously fluid and porous layers, *J. Fluid Mech.*, **186**, 257–284 (1988)
18 Arquis, E. and Caltagirone, J. P. Interacting convection between fluid and open porous layers, *ASME Paper No. 87–WA/HT-24*, 1–9 (1987)
19 Le Breton, P., Caltagirone, J. P. and Arquis, E. Natural convection in a square cavity with thin porous layers on its vertical walls, *Trans. ASME J. Heat Transfer*, **113**, 892–898 (1991)
20 Whitaker, S. The equations of motion in porous media, *Chem. Eng. Sci.*, **21**, 291–300 (1966)
21 Bear, J. *Dynamics of Fluids in Porous Media*, American Elsevier, New York (1972)
22 Bejan, A. *Convection Heat Transfer*, John Wiley, New York (1984)
23 Stevens, W. N. R. Finite element stream function – vorticity solution of steady laminar natural convection, *Int. J. Num. Meth. Fluids*, **2**, 349–366 (1982)